

MDPI

Article

Influence of Annealing on the Dielectric Properties of Zn-SiO₂/Si Nanocomposites Obtained in "Hot" Implantation Conditions

Tomasz N. Kołtunowicz ^{1,*}, Karolina Czarnacka ², Piotr Gałaszkiewicz ¹, Fadei F. Komarov ³, Maxim A. Makhavikou ³ and Oleg V. Milchanin ³

- Department of Electrical Devices and High Voltage Technology, Lublin University of Technology, 20-618 Lublin, Poland
- Department of Technology Fundamentals, University of Life Sciences in Lublin, 20-950 Lublin, Poland
- ³ Institute of Applied Physics Problems, Belarusian State University, 220030 Minsk, Belarus
- * Correspondence: t.koltunowicz@pollub.pl; Tel.: +48-81-538-47-13

Abstract: This paper presents the results of AC electrical measurements of Zn-SiO₂/Si nanocomposites obtained by ion implantation. Implantation of Zn ions was carried out into thermally oxidized p-type silicon substrates with energy of 150 keV and fluence of 7.5×10^{16} ion·cm⁻² at a temperature of 773 K, and is thus called implantation in "hot" conditions. The samples were annealed in ambient air for 60 min at 973 K. Electrical measurements of Zn-SiO₂/Si nanocomposites were carried out before and after annealing. Measurements were performed in the temperature range from 20 K to 375 K. The measurement parameters were the resistance R_p , the capacitance C_p , the phase shift angle θ and the tangent of loss angle $\tan \delta$, as a function of the frequency in the range from 50 Hz to 5 MHz. Based on the characteristics $\sigma(f)$ and the Jonscher power law before and after sample annealing, the values of the exponent s were calculated depending on the measurement temperature. Based on this, the conductivity models were matched. Additionally, the real and imaginary parts of the dielectric permittivity were determined, and on their basis, the polarization mechanisms in the tested material were also determined.

Keywords: nanocomposite; ion implantation; impedance spectroscopy; charge transport



Citation: Kołtunowicz, T.N.;
Czarnacka, K.; Gałaszkiewicz, P.;
Komarov, F.F.; Makhavikou, M.A.;
Milchanin, O.V. Influence of
Annealing on the Dielectric
Properties of Zn-SiO₂/Si
Nanocomposites Obtained in "Hot"
Implantation Conditions.
Nanomaterials 2022, 12, 3449. https://doi.org/10.3390/nano12193449

Academic Editor: Adriano Sacco

Received: 6 September 2022 Accepted: 29 September 2022 Published: 2 October 2022

Publisher's Note: MDPI stays neutral with regard to jurisdictional claims in published maps and institutional affiliations.



Copyright: © 2022 by the authors. Licensee MDPI, Basel, Switzerland. This article is an open access article distributed under the terms and conditions of the Creative Commons Attribution (CC BY) license (https://creativecommons.org/licenses/by/4.0/).

1. Introduction

Ion implantation is one of the most flexible methods of producing nanocomposites with metallic and semiconductor nanoparticles in the SiO₂ matrix due to high purity of the process, precise control of the implanted ions' fluence, the spatial distribution of implanted atoms, etc. [1–4]. However, the main advantage of this method is its full compatibility with modern silicon microelectronics. At high implantation fluences, the concentration of incorporated impurities in the matrix significantly exceeds the limit of equilibrium solubility, and the formation of nanoparticles occurs.

Compared to other techniques, such as chemical vapor deposition (CVD) [5], molecular beam epitaxy (MBE) [6], sol–gel synthesis [7] and pulsed laser deposition [8], ion implantation has several important advantages, including no synthesis-related impurities and precise control of the introduced metal ions and their depth distribution in the dielectric matrix [9]. Accordingly, nanoparticles of metals and metal oxides, such as copper (Cu) [10], gold (Au), nickel (Ni) [11], silver (Ag) [12], cobalt (Co) [13], etc., were synthesized by ion implantation in dielectrics such as SiO₂ [14], Al₂O₃ [15], and even in MgO [16,17] or CeO₂ [13]. According to the literature sources, in the SiO₂ matrix, the implanted ions form spherical nanoparticles with a random distribution [14]. In particular, zinc (Zn) and zinc oxide (ZnO) nanoparticles produced in SiO₂ by ion implantation are popular due to their present and possible applications in high-performance optoelectronics [18–20].

The dielectric properties of nanomaterials are important characteristics for their potential applications in capacitors, sensors and memory devices. The influence of frequency on

Nanomaterials 2022. 12, 3449 2 of 15

the dielectric behavior and AC conductivity of nanomaterials provides key information on the conductive phenomena in these materials [21,22]. It should be noted that the dielectric properties and electric transport of nanomaterials are different from the properties of materials on a micro- or macrometric scale, mainly due to an increase in the number of atoms or ions between phases, and also due to the fact that many structural defects are introduced in or near the grain boundaries. AC measurements of nanocomposites' electrical properties have been extensively conducted for granular metal–dielectric nanocomposites, with SiO_2 [23], Al_2O_3 [24,25], CaF_2 [26,27] and PZT [27–29] dielectrics used as matrix materials, and CoFeZr ferromagnetic alloy [24–29] and copper [23,30] used as nanofiller.

In this work, impedance spectroscopy was used to characterize and compare the electrical properties of a nanocomposite with the silicon oxide matrix in which metallic zinc nanograins (nanoclusters) were formed by ion implantation. As a result, it gives an opportunity to determine mechanisms of electric charge transfer in this material and to study other phenomena conditioned by these mechanisms.

2. Experimental

The initial SiO_2/p -type Si samples $2~cm \times 2~cm$ in size with an electrical resistivity of $10~\Omega \cdot cm$ for a silicon wafer were cut from thermally oxidized Si substrates. The thickness of the SiO_2 layer, as measured by transmission electron microscopy in cross-section geometry by an analytical electron microscope Hitachi H-800 operating at 200 keV, was about 600 nm. These samples were implanted at the temperature of 773 K with 150 keV-Zn ions to the fluence of $7.5 \times 10^{16}~ion \cdot cm^{-2}$. Therefore, this regime is called implantation in "hot" conditions. Afterwards, the samples were annealed at 973 K for 60 min in ambient air. Zn concentration depth distributions of the implanted and annealed samples were analyzed by Rutherford backscattering spectrometry (RBS) using 1.4 MeV He ions with a registration angle of 170 degrees. Information on depth distribution of Zn atoms' concentration was obtained by processing the RBS spectra using the SIMNRA software package [31].

The measured samples consisted of the p-type silicon substrate on which the 600 nm SiO_2 layers were formed by oxidation in dry ambient O_2 . After this process, the Zn^+ ion implantation was performed and a part of the samples was annealed.

A thin layer of silver paste was applied to the tested nanocomposite samples in order to avoid the negative impact of point contact during the measurements. Electrical measurements of $Zn-SiO_2/Si$ nanocomposites were carried out through the sample (in a capacitor system), so the contacts were placed on both sides of the sample, leaving a distance of approx. 1 mm from its edge.

It should also be mentioned that a part of implanted atoms can penetrate the SiO₂/Si interface due to radiation-enhanced diffusion in the process of ion implantation and sample annealing. However, a concentration of such Zn atoms in the tail part of depth distributions in Figure 1 is under the mentioned resolution of the RBS method (about 5×10^{18} at/cm³). Such a level of silicon dioxide doping can, to a significant degree, change the conductivity properties of this deep part of implanted oxide, as well.

Liquid helium cooling was applied using a cryostat. This made it possible to conduct measurements with temperature regulation with an accuracy of 0.002 K. Additionally, a vacuum chamber was used, in which the samples were mounted. It helped stabilize the temperature and prevent the samples from damping. Thus, the measurements were carried out in a vacuum at the level of 0.2 atm. The temperature in the chamber was cooled in a closed circuit using a helium compressor. The temperature control in the chamber was ensured by a silicon sensor, a LakeShore 335 temperature controller, and a heater located in the cryostat head connected to the controller. Measurements were performed in the temperature range from 20 K to 375 K, with the step of 2 K in the range of 20–40 K, with the step of 3 K in the range of 151–375 K.

Nanomaterials **2022**, 12, 3449 3 of 15

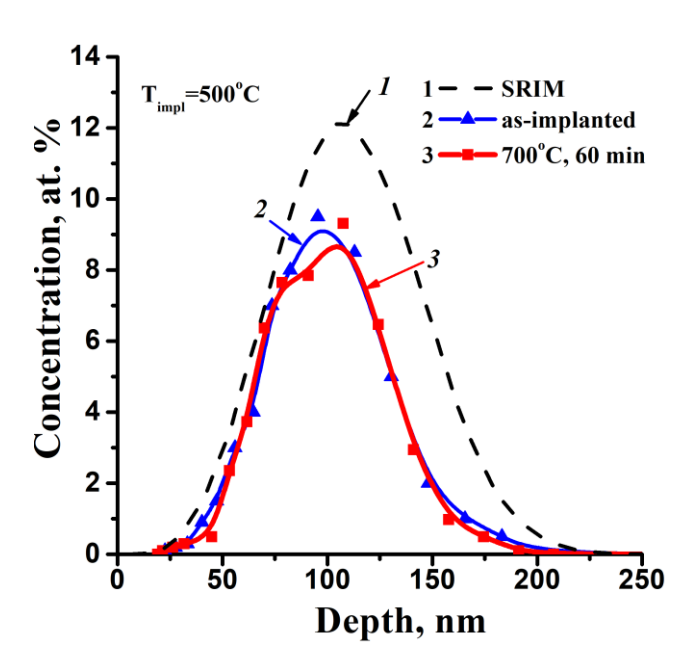


Figure 1. Simulated (SRIM-2013) (curve 1) and calculated from RBS spectra depth profiles of impurity concentration in SiO₂ after Zn⁺ implantation (150 keV, 7.5×10^{16} cm⁻²) (curve 2) and subsequent annealing at 973 K (700 °C) for 60 min (curve 3).

Measurements of electrical parameters were carried out using HIOKI impedance meters. The measurement parameters were the resistance R_p , capacitance C_p , the phase shift angle θ and the tangent of the loss angle $\tan \delta$, as a function of the frequency in the range of 50 Hz to 5 MHz. The test stand is controlled by a computer to which the meters and a temperature controller are connected. The measured results are saved on the computer's hard disk in xls format [32].

3. Results and Discussion

Figure 1 shows the simulated (SRIM'13 [33]) depth distribution profile of implanted Zn atoms and the profiles calculated from experimental RBS spectra. Computer simulation gave a Gaussian-type Zn concentration depth profile with a peak concentration of about 12 at % at the depth of \sim 113 nm in the oxide matrix (Figure 1, curve 1). "Hot" implantation into SiO₂ (Figure 1, curve 2) leads to a 1.3-fold reduction in the maximum impurity concentration in comparison with the computer simulation data. The impurity loss during ion implantation amounts to 38%. Annealing (973 K, 60 min) results in an insignificant diffusion of implanted impurity to the sample surface (Figure 1, curve 3).

Figure 2 shows the XTEM and HRTEM images (insets) of Zn nanoparticles embedded in the SiO_2 matrix. "Hot" implantation leads to the formation of small clusters just after zinc implantation (see Figure 2a). The absence of any nanoclusters in the subsurface region (up to 40 nm) of the SiO_2 layers proves the minor zinc atoms' diffusion to the surface at elevated temperatures up to 973 K. Underneath the cluster-free region, the layer with small clusters (2–15 nm) is located in the depth range of 40–200 nm.

The bigger clusters 10–15 nm in size are concentrated at the depth of 100–110 nm (nearly $R_{\rm p}$; $R_{\rm p}$ is the projected range of implanted atoms). The crystalline nature of the precipitates is proved by the presence of Moiré contrast in the HRTEM images (see Figure 2a,b, insets). The interplanar spacing 2.12 Å measured for dark contrast precipitate (Figure 2a, inset) is in agreement with the tabulated value of 2.09 Å for the (101) planes of the hexagonal Zn. Heat treatment at 973 K for 60 min (Figure 2b) results in a substantial structural transformation of the implanted layer. One can see two spatial separated layers. The small Zn nanoparticles surrounded by the oxide shells (see Figure 2b, inset) at the depth range of 30–100 nm should be noted. The calculated value of the interplanar spacing of the oxide shells is 1.91 Å. It corresponds to the distance between (102) planes of the hexagonal ZnO

Nanomaterials **2022**, 12, 3449 4 of 15

phase. In addition, the formation of voids is observed at the "Zn nanocluster–SiO₂ matrix" interface (Figure 2b, shown by arrows).

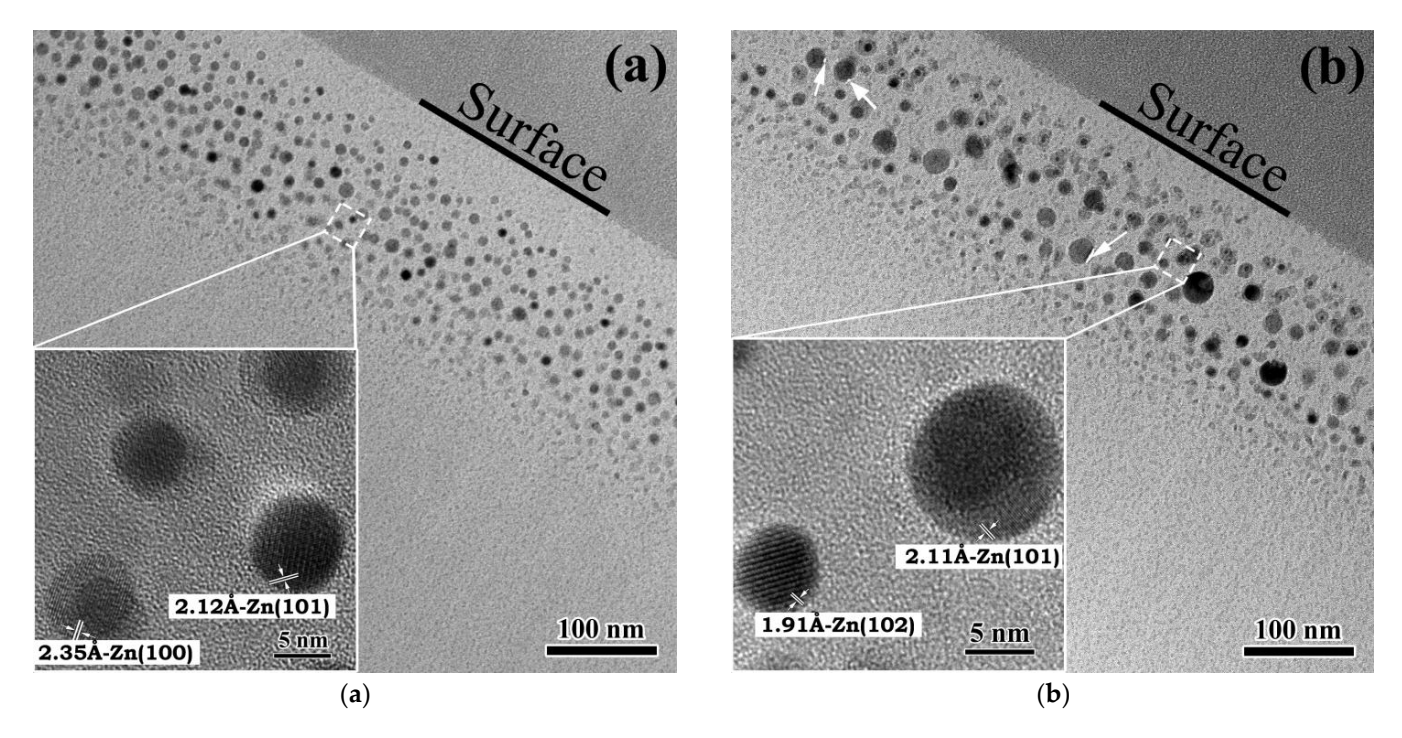


Figure 2. XTEM images of SiO₂ (600 nm)/Si samples implanted with Zn⁺ (150 keV, 7.5×10^{16} ions/cm²): (a) as-implanted sample, and the samples after annealing at 973 K for (b) 60 min. The insets depict the HRTEM nanoparticle images.

Figure 3 shows the temperature–frequency dependence of the Zn-SiO₂/Si nanocomposite conductivity immediately after implantation at the temperature $T_{\rm impl}$ = 773 K with 150 keV-Zn ions to the fluence of 7.5×10^{16} ion/cm². In the range of lower frequencies, a weak conductivity dependence on frequency can be seen, corresponding to the DC conductivity $\sigma_{\rm dc}$. In this frequency range, a strong temperature dependence characteristic is observed for dielectric conductivity. At the same time, as the temperature rises, the plateau of DC conductivity extends to higher frequencies. With a further increase in frequency, the conductivity increases significantly (almost 5–6 orders of magnitude), but shows a poor temperature dependence. Such a conductivity behavior with frequency may indicate a hopping mechanism of charge transfer in the tested material [34–36]. The increase in AC conductivity with frequency is due to the relaxation of moving electrons. As the frequency increases, the charge carriers are forced to jump between the located states, which causes a decrease in activation energy.

Figure 4 shows the Arrhenius dependence for conductivity determined at the frequency f = 100 Hz. The diagram presents three ranges of change in conductivity with temperature, which may indicate at least two ways of the charge transporting in the tested material. In the range of low temperatures, to approx. 35 K, the conductivity is practically constant and does not show an activating character. It is related to the carrier hopping near the Fermi level $E_{\rm F}$. In the range from 35 K to about 135 K, conductivity changes are non-linear and it is difficult to determine the electron activation energy on the basis of the Arrhenius law. In the range of high temperatures, a linear change in conductivity with temperature is visible, which fulfills the Arrhenius law, making it possible to calculate the activation energy of the conductivity. Its value is approximately $\Delta E_1 \approx 0.037$ eV. This confirms the presence of a thermally activated hopping conductivity [22,23].

Nanomaterials **2022**, 12, 3449 5 of 15

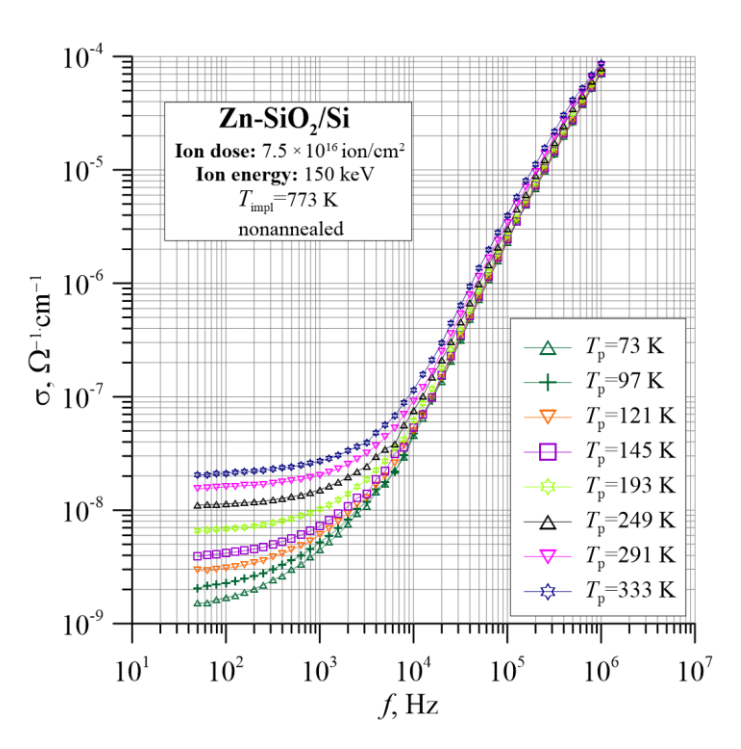


Figure 3. Temperature–frequency dependence of the conductivity $\sigma(f, T_p)$ for the Zn-SiO₂/Si nanocomposite immediately after preparation under "hot" implantation conditions (150 keV, 7.5×10^{16} ion/cm², $T_{\rm impl}$ = 773 K).

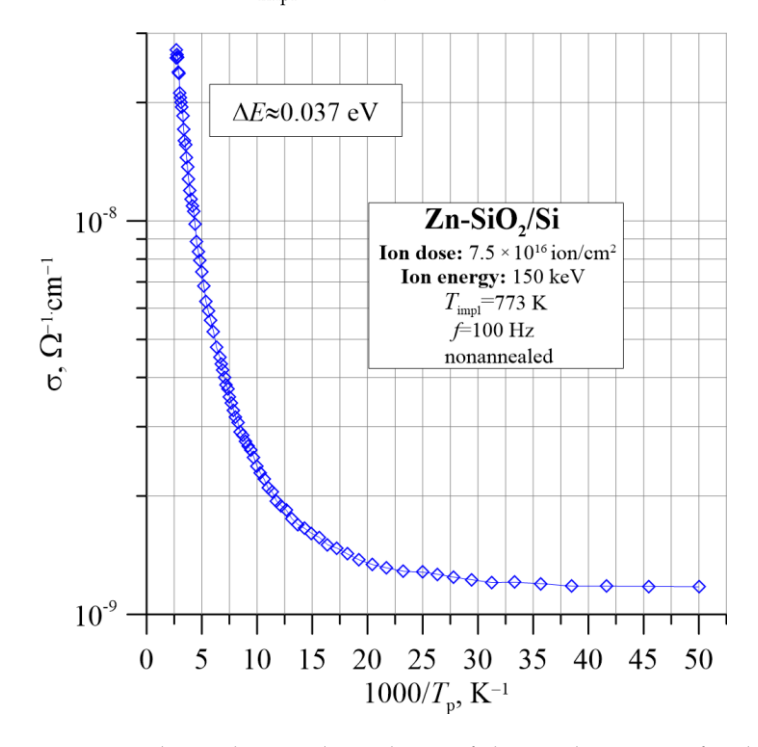


Figure 4. The Arrhenius dependence of the conductivity σ for the Zn-SiO₂/Si nanocomposite immediately after preparation under "hot" implantation conditions (150 keV, 7.5 \times 10¹⁶ ion/cm², T_{impl} = 773 K).

Figures 5–7 show the dielectric properties of the tested Zn-SiO₂/Si nanocomposite, which were measured in the frequency range from 50 Hz to 5 MHz at temperatures from 20 K to 375 K. The real dielectric component ε_r shows a sharp decrease with frequency in the low and high frequencies. In the range of intermediate frequencies, ε_r decreases slightly or is practically constant. Accordingly, the imaginary part of the dielectric permittivity ε'' in the low- and intermediate-frequency ranges rapidly decreases with increasing frequency,

Nanomaterials **2022**, 12, 3449 6 of 15

reaching a Debye-like relaxation peak at angular frequencies of about 4×10^6 rad/s. The low-frequency section of the ϵ'' relationship is related to the DC conductivity. The tangent of the dielectric loss angle $\tan\delta$ is high, with a temperature-dependent minimum ranging from 6×10^{-3} to 2×10^{-2} at a frequency of about 10^4 Hz. ϵ_r and ϵ'' frequency dependencies are used later in this work to determine the Cole–Cole relationship.

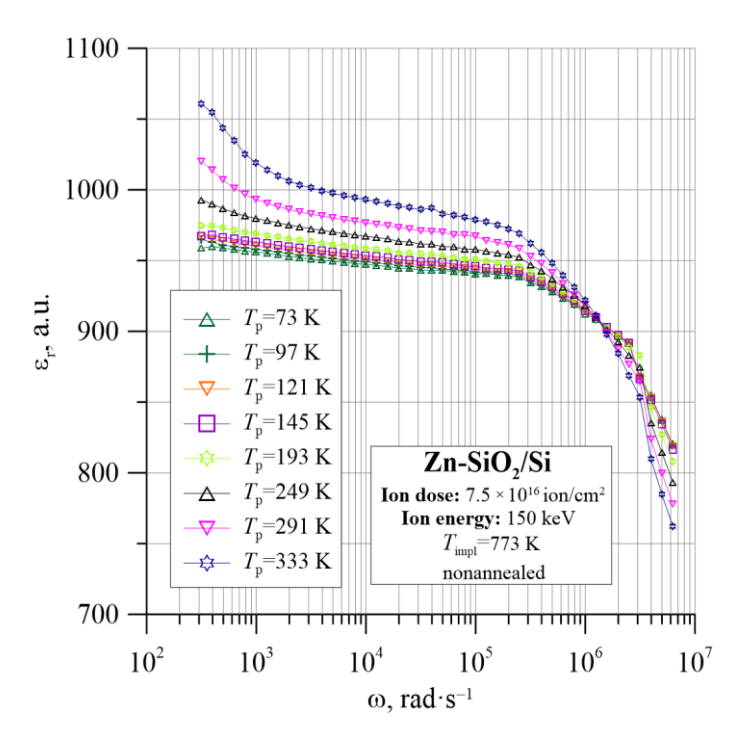


Figure 5. Temperature dependence of the real part of dielectric permittivity ε_r for the Zn-SiO₂/Si nanocomposite immediately after preparation under "hot" implantation conditions (150 keV, 7.5 × 10^{16} ion/cm², T_{impl} = 773 K).

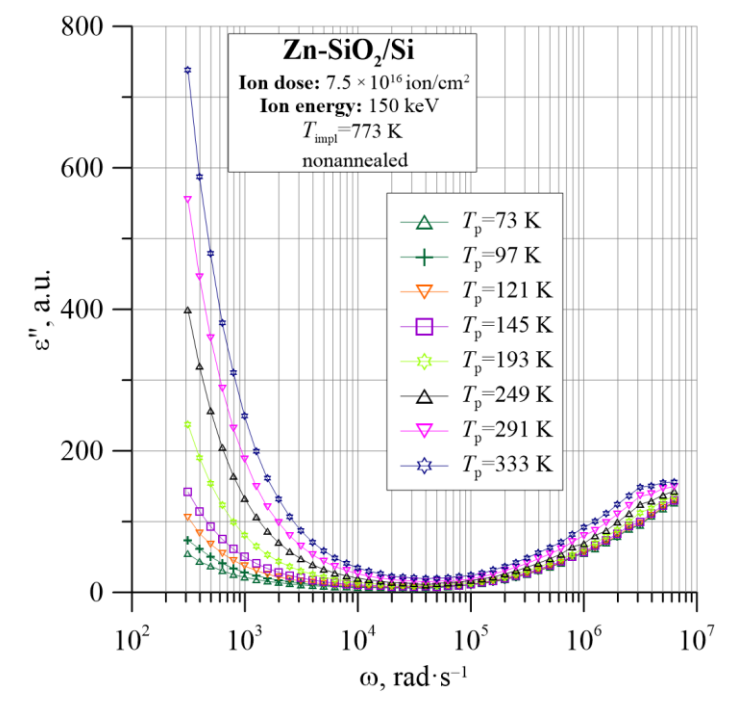


Figure 6. Temperature dependence of the imaginary part of dielectric permittivity ε'' for the Zn-SiO₂/Si nanocomposite immediately after preparation under "hot" implantation conditions (150 keV, 7.5×10^{16} ion/cm², $T_{\rm impl}$ = 773 K).

Nanomaterials **2022**, 12, 3449 7 of 15

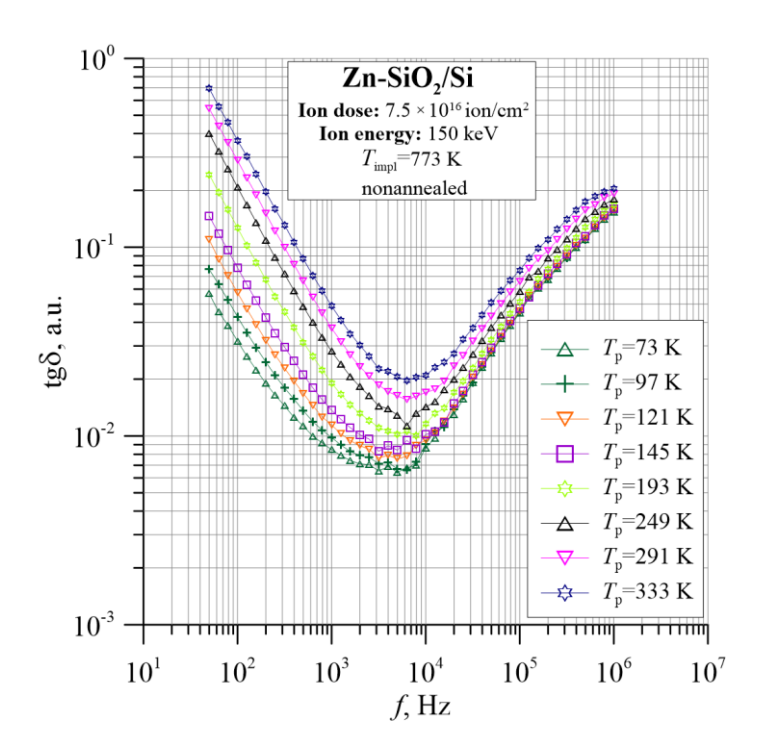


Figure 7. Temperature dependence of the tangent of dielectric loss angle $tg\delta$ for the Zn-SiO₂/Si nanocomposite immediately after preparation under "hot" implantation conditions (150 keV, 7.5 × 10^{16} ion/cm², T_{impl} = 773 K).

Figures 8 and 9 show the frequency–temperature dependences of the capacitance C_p and the phase shift angle θ . On their basis, it can be concluded that the material has a capacitive character because the C_p dependence is practically independent of frequency and temperature. Moreover, the phase shift angle in the entire measuring range is negative. Additionally, the angle θ in the range of low frequencies decreases, reaching a value close to -90° , which is characteristic of the parallel RC circuit.

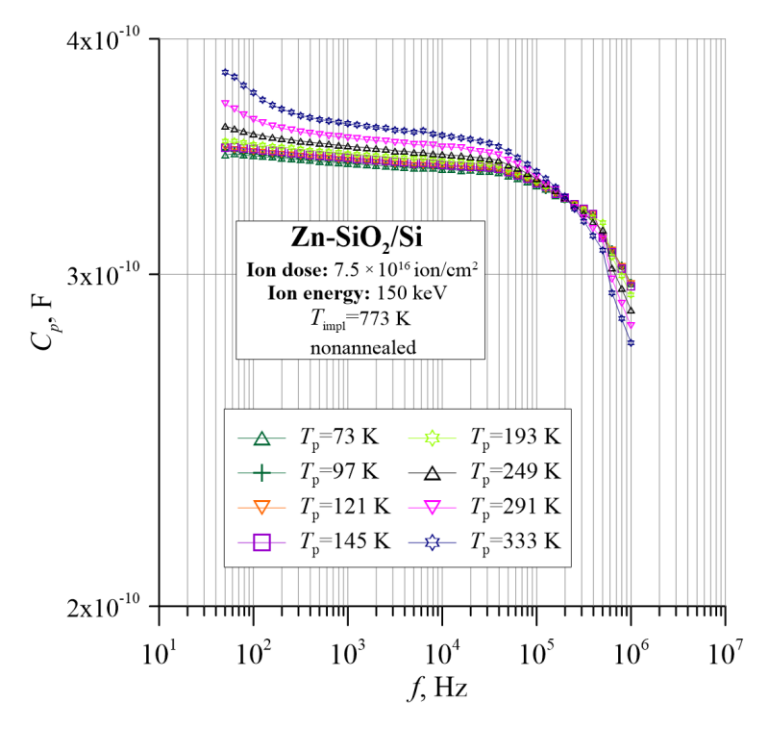


Figure 8. Temperature dependence of the capacitance C_p for the Zn-SiO₂/Si nanocomposite immediately after preparation under "hot" implantation conditions (150 keV, 7.5×10^{16} ion/cm², $T_{\text{impl}} = 773$ K).

Nanomaterials **2022**, 12, 3449 8 of 15

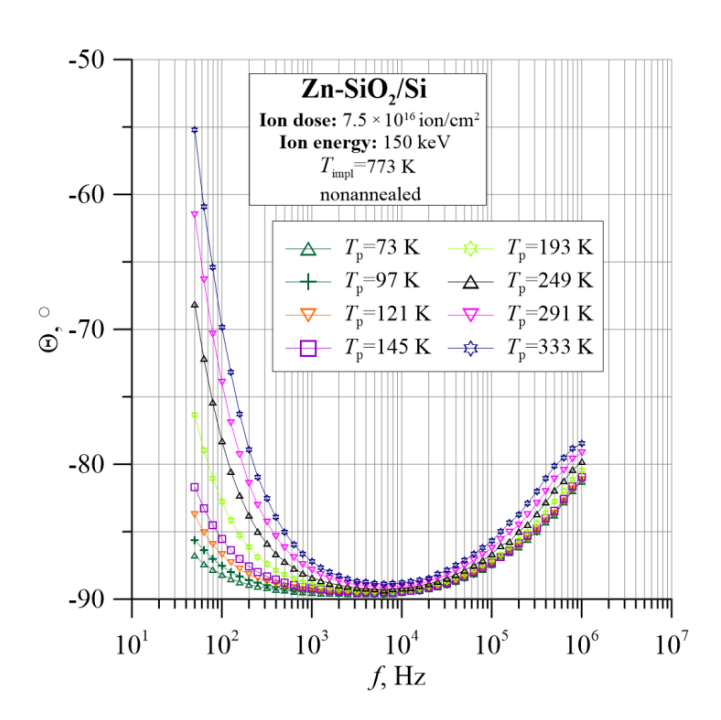


Figure 9. Temperature dependence of the phase shift angle θ for the Zn-SiO₂/Si nanocomposite immediately after preparation under "hot" implantation conditions (150 keV, 7.5 \times 10¹⁶ ion/cm², $T_{\rm impl}$ = 773 K).

The situation changes significantly after annealing. Figure 10 shows a graph of the temperature–frequency dependence of the conductivity for the Zn-SiO $_2$ /Si sample obtained in the "hot" implantation conditions subjected to annealing at 974 K in ambient air for 60 min. The increase in conductivity with a frequency of up to 6 orders of magnitude is clearly visible. However, in the low- and medium-frequency range, the conductivity does not show an orderly dependence on temperature. This can be seen in the Arrhenius graphs of conductivity shown in Figure 11. Only in the high-frequency range, the conductivity increases with temperature, showing dielectric conduction behavior.

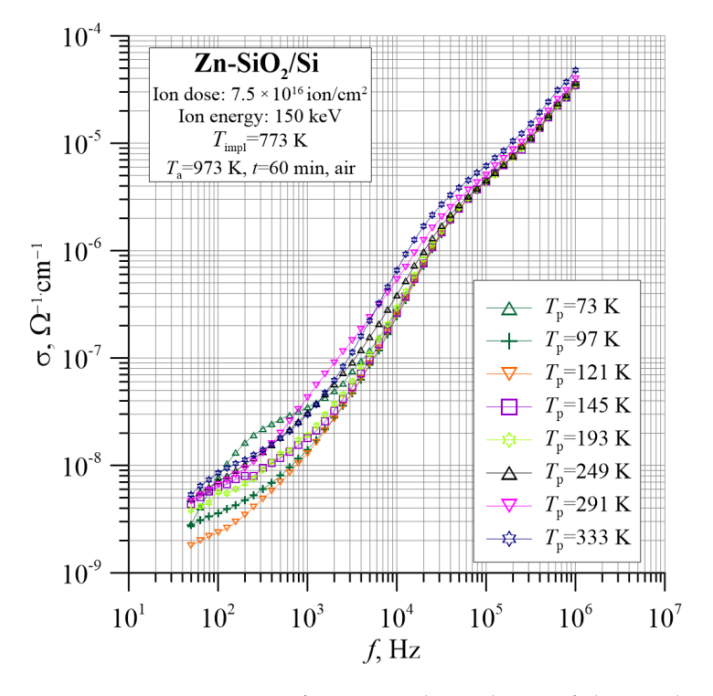


Figure 10. Temperature–frequency dependence of the conductivity $\sigma(f, T_p)$ for the Zn-SiO₂/Si nanocomposite prepared under "hot" implantation conditions (150 keV, 7.5 \times 10¹⁶ ion/cm², $T_{\text{impl}} = 773$ K) after annealing.

Nanomaterials **2022**, 12, 3449 9 of 15

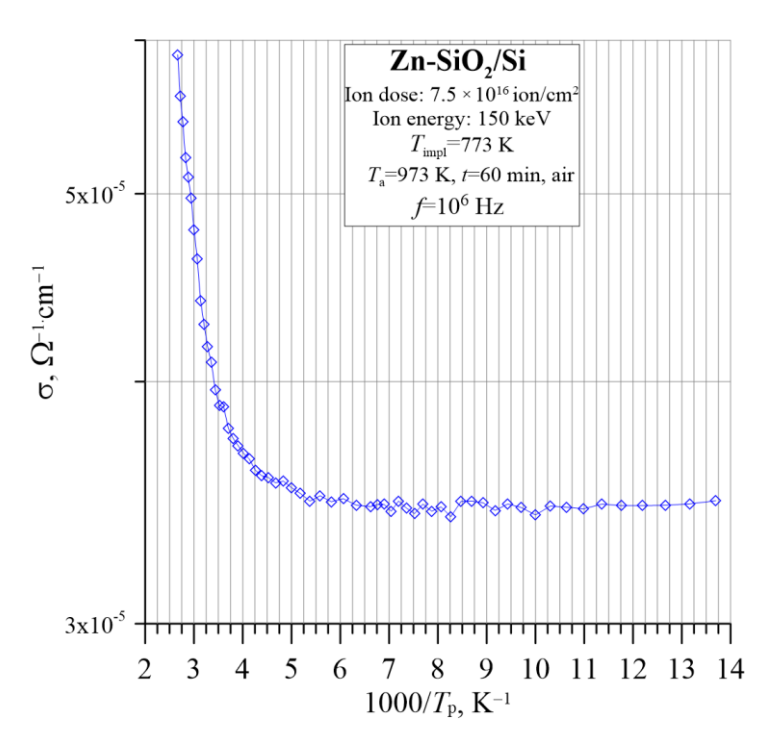


Figure 11. The Arrhenius dependence of the conductivity σ for the Zn-SiO₂/Si nanocomposite prepared under "hot" implantation conditions (150 keV, 7.5×10^{16} ion/cm², $T_{\text{impl}} = 773$ K) after annealing for frequency $f = 10^6$ Hz.

At high frequencies (Figure 11), three ranges of conductivity change with temperature can be distinguished. The first one is up to approx. 200 K, where the conductivity does not depend on the measurement temperature and is related to the hopping of carriers near the Fermi level $E_{\rm F}$. The second one is at temperatures up to approx. 280 K, where changes in conductivity are non-linear. The third region of high temperatures is above 280 K, where there is a linear change according to the Arrhenius law. In this temperature range, it was possible to determine the thermal activation energy of electrons, and it amounts to $\Delta E_2 \approx 0.060$ eV.

This theory is confirmed by the temperature–frequency dependencies of the dielectric parameters shown in Figures 12–16. The tangent of the dielectric loss angle $\tan\delta$ (Figure 12) changes parabolically with the frequency, which indicates a relaxation loss mechanism.

Figure 13 shows the frequency–temperature dependence of the real ϵ_r (Figure 13a) and the imaginary ϵ'' (Figure 13b) components of dielectric permittivity. The analysis of these graphs proves the hopping charge transfer between the closest neighbors, creating electric dipoles.

First, there is a characteristic maximum in the graph $\varepsilon''(f)$ in the frequency range above 10^5 Hz. Second, the frequency at which the peak occurs has the same value as the inflection frequency of the descending curve $\varepsilon_r(f)$, as shown in Figure 13a. Additionally, in the range of low frequencies, the permeability ε'' shows another polarization mechanism, which is especially visible for the lowest temperatures. A second relaxation peak appears which, at higher temperatures, is likely to occur at lower frequencies than the measuring range. In the case of the annealed sample, the decrease in ε_r with frequency is not related to the DC conductivity (as in the case of a nonannealed sample), because the characteristic $\sigma(f)$ shows a strong frequency dependence also in the lowest range. It is more likely that there is a space charge polarization according to the Maxwell–Wagner model at the metal–dielectric interface for larger metallic nanoparticles and at the dielectric–silicon substrate interface. Relaxation according to this mechanism requires higher activation energies and a longer time (i.e., low frequency). A comparison of the real and imaginary dielectric permeability as a function of frequency measured at $T_p = 333$ K is shown in Figure 14.

Nanomaterials **2022**, 12, 3449 10 of 15

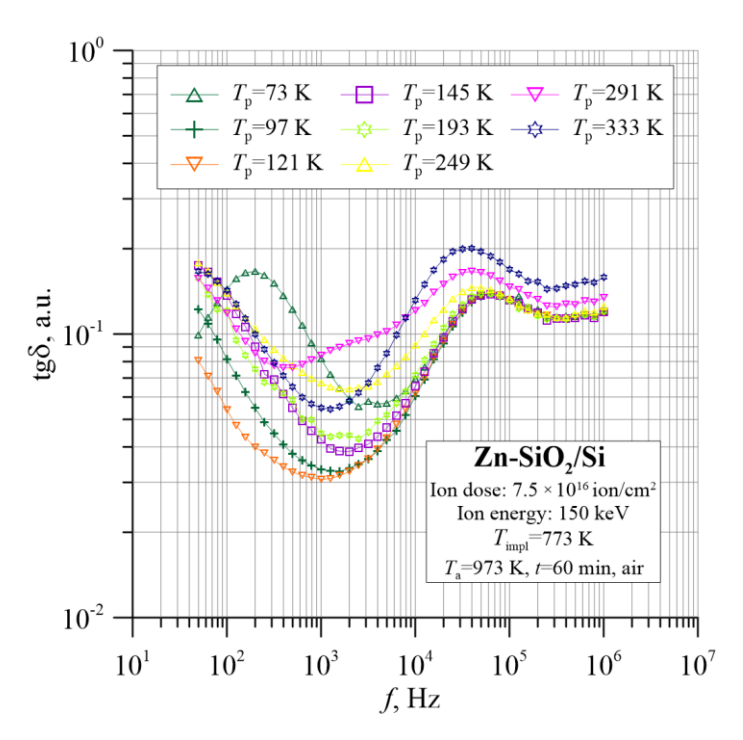


Figure 12. Temperature–frequency dependence of the tangent of dielectric loss angle $tg\delta(f, T_p)$ for the Zn-SiO₂/Si nanocomposite prepared under "hot" implantation conditions (150 keV, 7.5×10^{16} ion/cm², T_{impl} = 773 K) after annealing.

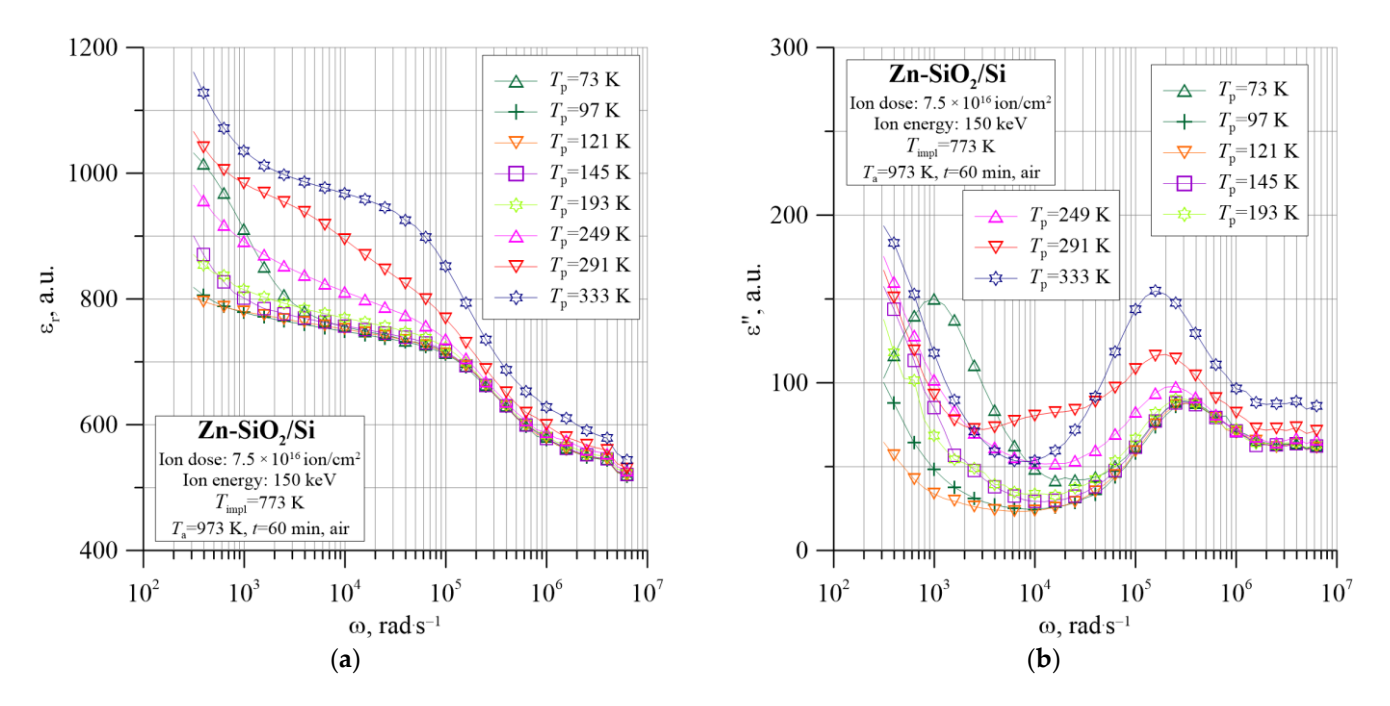


Figure 13. Temperature–frequency dependence of the real (a) and imaginary (b) part of dielectric permittivity for the Zn-SiO₂/Si nanocomposite prepared under "hot" implantation conditions (150 keV, 7.5×10^{16} ion/cm², $T_{impl} = 773$ K) after annealing.

Nanomaterials **2022**, 12, 3449 11 of 15

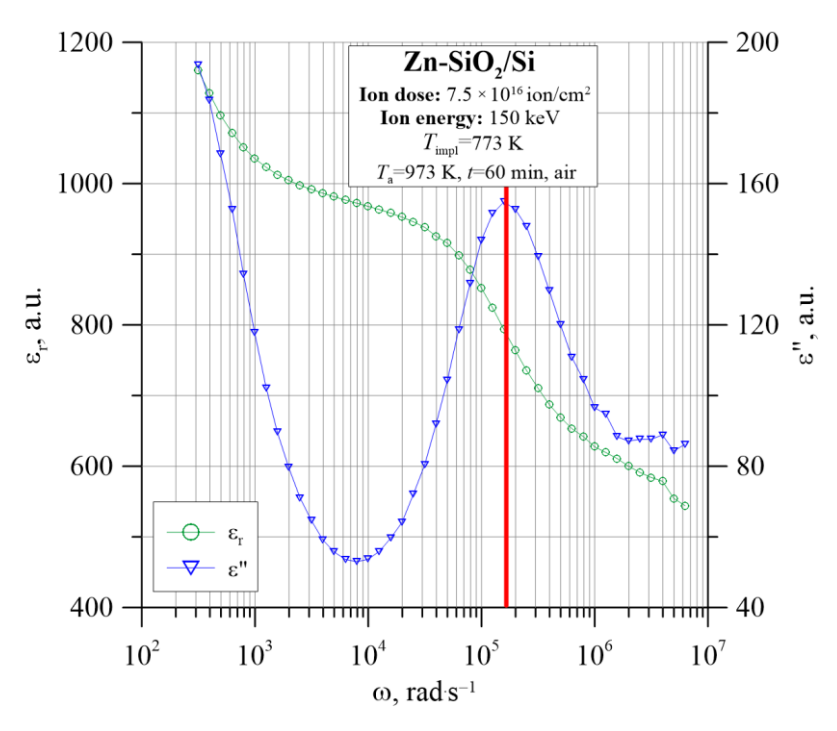


Figure 14. Comparison of the real and imaginary dielectric permittivity as a function of frequency measured at $T_p = 333$ K.

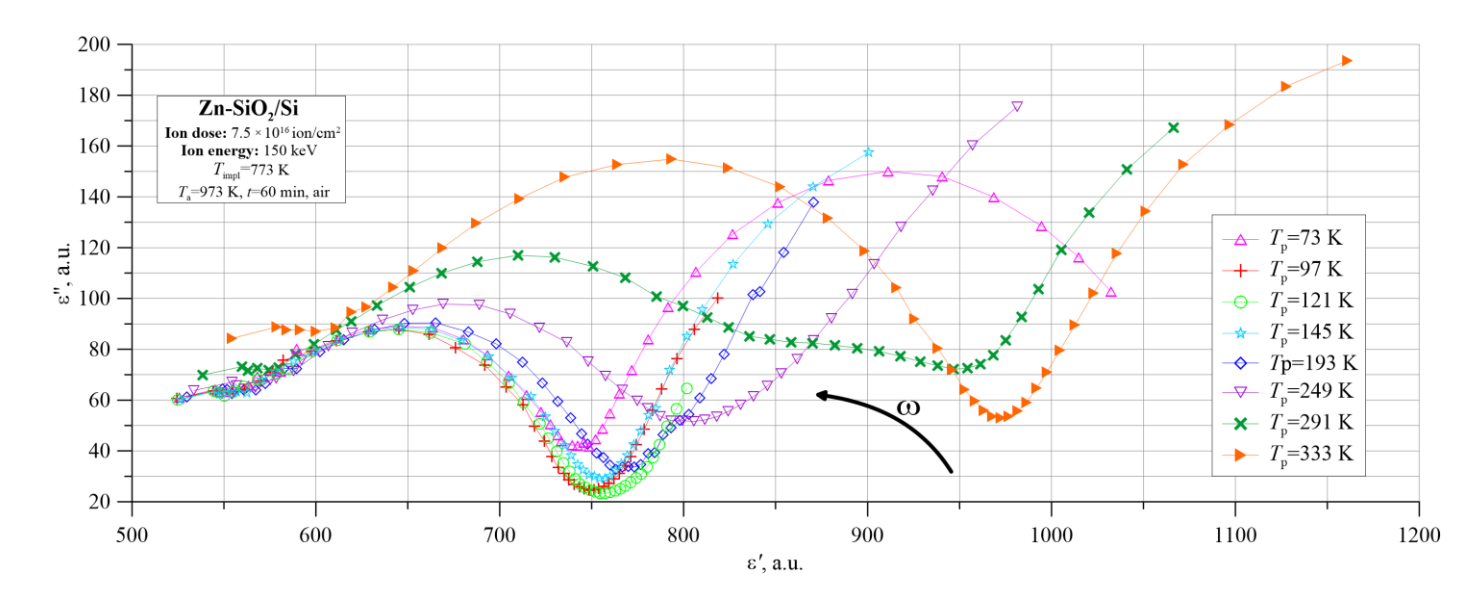


Figure 15. Cole–Cole diagram of Zn-SiO₂/Si nanocomposite obtained in the conditions of "hot" implantation (150 keV, 7.5×10^{16} ion/cm², $T_{impl} = 773$ K) and annealed at the temperature of $T_a = 973$ K.

Nanomaterials **2022**, 12, 3449

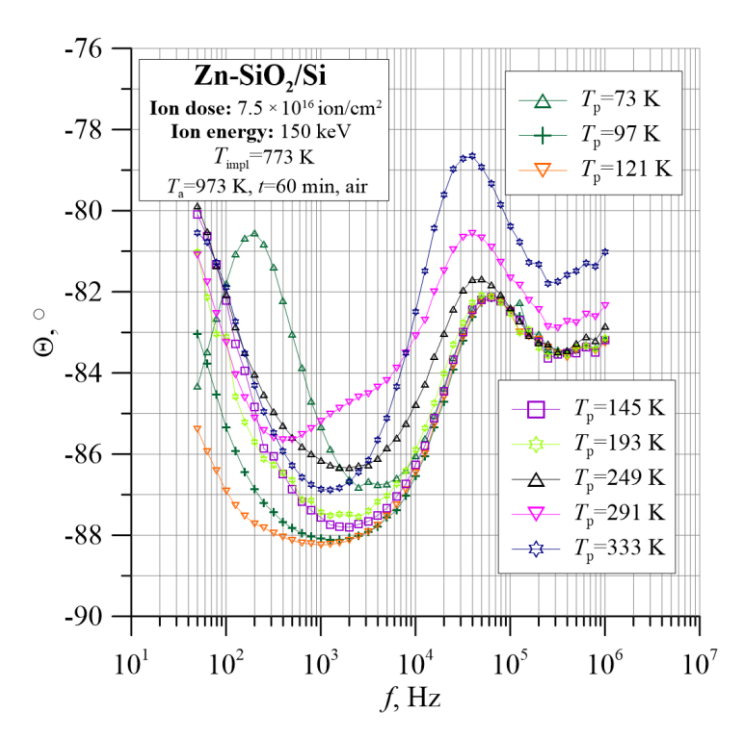


Figure 16. Temperature–frequency dependence of phase shift angle $\theta(f, T_p)$ for the Zn-SiO₂/Si nanocomposite prepared under "hot" implantation conditions (150 keV, 7.5 × 10¹⁶ ion/cm², $T_{\text{impl}} = 773 \text{ K}$) after annealing.

This phenomenon is clearly visible in the Cole–Cole diagrams presented in Figure 15. For the entire temperature range, characteristic semi-circles corresponding to the electric dipoles' creation due to hopping charge transfer between the closest neighbors are visible, and in the lower frequency range, fragments of the semi-circle can be seen, confirming the Maxwell–Wagner model occurring at low frequencies. At the lowest temperatures, two characteristic semicircles are visible, corresponding to the peaks in the graph $\varepsilon''(f)$.

The analysis of the tested sample is complemented by information about its capacitive behavior, as shown in Figures 16 and 17. In the diagram of the frequency–temperature dependence of the capacitance (Figure 17), the capacitance at the lowest frequencies decreases sharply, and then its value decreases gently, and then decreases again abruptly. This is related to the previously described mechanisms of polarization in the material. Additionally, the phase shift angle presented in Figure 16 shows negative values over the entire measuring range, which proves the capacitive nature of the material.

Nanomaterials **2022**, 12, 3449

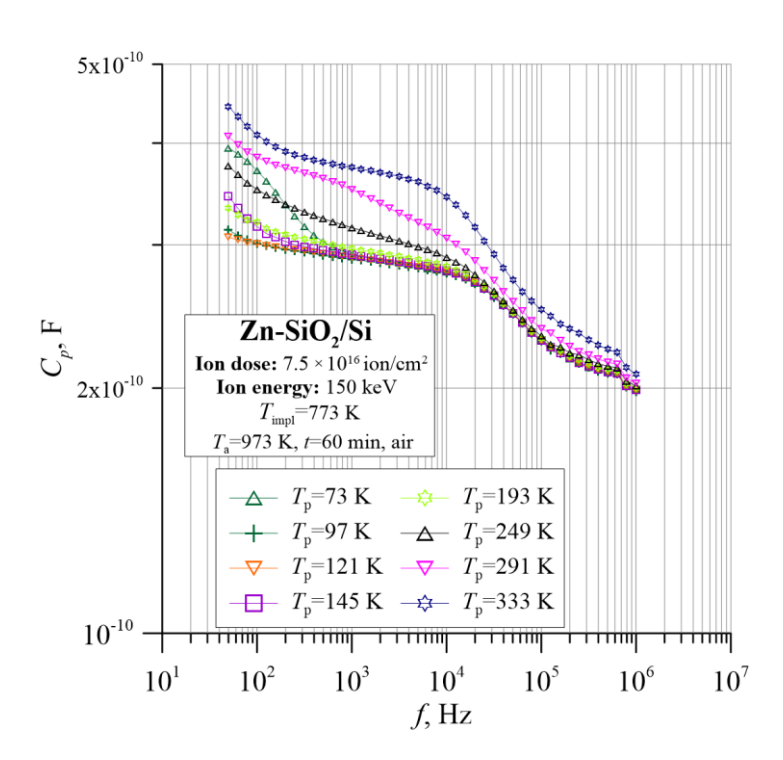


Figure 17. Temperature–frequency dependence of capacity $C_p(f, T_p)$ for the Zn-SiO₂/Si nanocomposite prepared under "hot" implantation conditions (150 keV, 7.5 × 10¹⁶ ion/cm², T_{impl} = 773 K) after annealing.

4. Conclusions

A series of Zn-SiO₂ nanocomposites produced by the implantation of Zn ions into the SiO₂/Si substrate was selected for analysis, which was carried out with ion energy of 150 keV and fluence of 7.5×10^{16} ion·cm⁻² at a temperature of $T_{\rm impl}$ = 773 K. Due to the high temperature of the process, it was described as implantation in "hot" conditions. The samples were annealed in ambient air for 60 min at a temperature of 973 K. The AC measurements were carried out in the temperature range from 20 K to 373 K and in the frequency range from 50 Hz to 1 MHz.

Before annealing, the conductivity increases with increasing frequency by almost 6 orders of magnitude. Based on this, the conductivity model was matched. According to the model, dipoles are formed, which change their orientation under the influence of further electron hops. The analysis of Arrhenius plots of conductivity for the frequency of 100 Hz showed that at temperatures below 35 K, electron hopping takes place near the Fermi level. In the temperature range above 200 K, the conductivity increases linearly with increasing temperature. This is evidence of thermally activated electron hopping.

The annealing of the Zn-SiO₂/Si nanocomposite sample at the temperature of 973 K caused significant changes in the nature of the $\sigma(f)$ dependence. Three ranges for the change in the slope of the almost rectilinear portions of the $\sigma(f)$ curve are visible.

The nature of the tangent of the dielectric loss angle as a function of the frequency of the nanocomposite sample, both before and after annealing, confirms the occurrence of the relaxation loss mechanisms in the tested material. The analysis of frequency–temperature diagrams of the real ϵ_r and imaginary ϵ'' component of dielectric permittivity proves the hopping model of charge transfer. It is related to the hopping charge transfer between the closest neighbors' potential wells and the creation of electric dipoles. In the case of an annealed sample, there is an additional low-frequency space charge polarization at the metal–dielectric interface for larger metallic precipitates and at the dielectric–silicon substrate interface according to the Maxwell–Wagner model. The Zn-SiO $_2$ /Si nanocomposite obtained in the conditions of "hot" implantation in the entire temperature and frequency range shows a capacitive nature.

Nanomaterials **2022**, 12, 3449 14 of 15

Author Contributions: Conceptualization, T.N.K. and K.C.; methodology, T.N.K., K.C., P.G., F.F.K., M.A.M. and O.V.M.; software, T.N.K. and K.C.; validation, T.N.K. and K.C.; formal analysis, T.N.K., K.C., P.G., F.F.K., M.A.M. and O.V.M.; investigation, K.C. and P.G.; resources, T.N.K., K.C. and F.F.K.; data curation, K.C.; writing—original draft preparation, T.N.K., K.C. and F.F.K.; writing—review and editing, T.N.K., K.C. and F.F.K.; visualization, T.N.K., K.C., P.G., M.A.M. and O.V.M.; supervision, T.N.K.; funding acquisition, T.N.K. All authors have read and agreed to the published version of the manuscript.

Funding: This research was supported by a subsidy from the Ministry of Education and Science (Poland) for the Lublin University of Technology as funds allocated for activities in the scientific disciplines of automation, electronics and electrical engineering (grant FD-20/EE-2/703).

Data Availability Statement: Not applicable.

Conflicts of Interest: The authors declare no conflict of interest.

References

 Meldrum, A.; Boatner, L.A.; White, C.W. Nanocomposites formed by ion implantation: Recent developments and future opportunities. Nucl. Instrum. Methods Phys. Res. Sect. B Beam Interact. Mater. At. 2001, 178, 7–16. [CrossRef]

- 2. De Julián Fernández, C.; Tagliente, M.A.; Mattei, G.; Sada, C.; Bello, V.; Maurizio, C.; Battaglin, G.; Sangregorio, C.; Gatteschi, D.; Tapfer, L.; et al. Structural and magnetic properties of Fe-Al silica composites prepared by sequential ion implantation. *Nucl. Instrum. Methods Phys. Res. Sect. B Beam Interact. Mater. At.* 2004, 216, 245–250. [CrossRef]
- 3. Liu, Z.; Yang, M.; Chen, T.P.; Liu, Y.; Zhang, H.Y. Dielectric engineering of Ge nanocrystal/SiO₂ nanocomposite thin films with Ge ion implantation: Modeling and measurement. *Mater. Des.* **2015**, *83*, 713–718. [CrossRef]
- 4. Nikolova, L.; Saint-Jacques, R.G.; Dahmoune, C.; Ross, G.G. Si nanoparticle formation in SiO₂ by Si ion implantation: Effect of energy and fluence on size distribution and on SiO₂ composition. *Surf. Coat. Technol.* **2009**, 203, 2501–2505. [CrossRef]
- 5. Avril, L.; Bourgeois, S.; De Lucas, M.M.; Domenichini, B.; Simon, P.; Addou, F.; Boudon, J.; Potin, V.; Imhoff, L. Thermal stability of Au-TiO₂ nanocomposite films prepared by direct liquid injection CVD. *Vacuum* **2015**, *122*, 314–320. [CrossRef]
- 6. Ge, F.; Bai, L.; Wu, W.; Cao, L.; Wang, X.; Ma, Y.; Han, S.; Wang, H.; An, X.; Wang, H.; et al. The controllable growth of CoBaTiO₃ nanocomposite epitaxial film by laser molecular beam epitaxy. *J. Cryst. Growth* **2010**, *312*, 2489–2493. [CrossRef]
- 7. Xie, J.; Yao, M.; Gao, W.; Su, Z.; Yao, X. Significantly enhanced dielectric constant and energy density in Au/Al₂O₃ nanocomposite thin films. *J. Alloys Compd.* **2019**, 772, 324–331. [CrossRef]
- 8. Lambert, M.; May, A.; Akkan, C.K.; Agarwal, N.; Aktas, O.C. Ag-Al₂O₃ optical nanocomposites with narrow particle size distribution prepared by pulsed laser deposition. *Mater. Lett.* **2014**, *137*, 405–408. [CrossRef]
- 9. Salvadori, M.C.; Teixeira, F.S.; Sgubin, L.G.; Cattani, M.; Brown, I.G. Surface modification by metal ion implantation forming metallic nanoparticles in an insulating matrix. *Appl. Surf. Sci.* **2014**, *310*, 158–163. [CrossRef]
- 10. Amekura, H.; Kono, K.; Takeda, Y.; Kishimoto, N. Cupric oxide nanoparticles in SiO₂ fabricated by copper-ion implantation combined with thermal oxidation. *Appl. Phys. Lett.* **2005**, *87*, 153105. [CrossRef]
- 11. Zhang, X.J.; Wang, Y.H.; Chen, H.J.; Zheng, L.R. Local structure study of the Ni nanoparticles embedded in SiO₂ by ion implantation. *J. Alloys Compd.* **2016**, 654, 176–179. [CrossRef]
- 12. Carles, R.; Farcău, C.; Bonafos, C.; Benassayag, G.; Pécassou, B.; Zwick, A. The synthesis of single layers of Ag nanocrystals by ultra-low-energy ion implantation for large-scale plasmonic structures. *Nanotechnology* **2009**, 20, 355305. [CrossRef]
- 13. Kumar, P.; Ahmad, B.; Chand, F.; Asokan, K. Magnetic and electronic structures of Co ion implanted CeO₂ thin films. *Appl. Surf. Sci.* **2018**, 452, 217–222. [CrossRef]
- 14. Salh, R.; Kourkoutis, L.F.; Zamoryanskaya, M.V.; Schmidt, B.; Fitting, H.J. Ion implantation and cluster formation in silica. Superlattices Microstruct. 2009, 45, 362–368. [CrossRef]
- 15. Spirin, R.E.; Salvadori, M.C.; Teixeira, F.S.; Sgubin, L.G.; Cattani, M.; Brown, I.G. Nanocomposite formed by titanium ion implantation into alumina. *J. Appl. Phys.* **2014**, *116*, 184306. [CrossRef]
- 16. Bachiller-Perea, D.; Debelle, A.; Thomé, L.; Behar, M. Damage accumulation in MgO irradiated with MeV Au ions at elevated temperatures. *J. Nucl. Mater.* **2016**, *478*, 268–274. [CrossRef]
- 17. Singh, J.P.; Lim, W.C.; Lee, J.; Song, J.; Lee, I.J.; Chae, K.H. Surface and local electronic structure modification of MgO film using Zn and Fe ion implantation. *Appl. Surf. Sci.* **2018**, 432, 132–139. [CrossRef]
- 18. Stepanov, A.L. Ion synthesis and nonlinear optical properties of metal nanoparticles. In *ICONO* 2010: *International Conference on Coherent and Nonlinear Optics*; Fabre, C., Zadkov, V., Drabovich, K., Eds.; SPIE: Bellingham, WA, USA, 2010; Volume 7993, p. 8.
- 19. Shen, Y.; He, W.; Zhang, D.; Zhang, X.; Xue, Y.; Liu, C. Creation of nanoparticles and luminescence in Al₂O₃ crystal by Zn ion implantation. *J. Lumin.* **2011**, *131*, 2725–2729. [CrossRef]
- Zatsepin, D.A.; Zatsepin, A.F.; Boukhvalov, D.W.; Kurmaev, E.Z.; Pchelkina, Z.V.; Gavrilov, N.V. Electronic structure and photoluminescence properties of Zn-ion implanted silica glass before and after thermal annealing. J. Non-Cryst. Solids 2016, 432, 183–188. [CrossRef]

Nanomaterials **2022**, 12, 3449 15 of 15

21. Gefle, O.S.; Lebedev, S.M.; Pokholkov, Y.P.; Tkachenko, S.N.; Volokhin, V.A.; Cherkashina, E.I. Study of dielectric relaxation spectra of composite materials by the dielectric spectroscopy method. In Proceedings of the 2005 International Symposium on Electrical Insulating Materials, Kitakyushu, Japan, 5–9 June 2005; pp. 85–87.

- Zukowski, P.; Koltunowicz, T.N.; Czarnacka, K.; Fedotov, A.K.; Tyschenko, I.E. Carrier transport and dielectric permittivity of SiO₂ films containing ion-beam synthesized InSb nanocrystals. J. Alloys Compd. 2020, 846, 156482. [CrossRef]
- 23. Koltunowicz, T.N.; Zukowski, P.; Czarnacka, K.; Bondariev, V.; Boiko, O.; Svito, I.A.; Fedotov, A.K. Dielectric properties of nanocomposite (Cu)_x(SiO₂)_(100-x) produced by ion-beam sputtering. *J. Alloys Compd.* **2015**, *652*, 444–449. [CrossRef]
- 24. Zukowski, P.; Kołtunowicz, T.; Partyka, J.; Fedotova, Y.A.; Larkin, A.V. Electrical properties of nanostructures (CoFeZr)_x + (Al₂O₃)_{1-x} with use of alternating current. *Vacuum* **2009**, *83*, S275–S279. [CrossRef]
- 25. Zhukowski, P.; Kołtunowicz, T.N.; Fedotova, J.A.; Larkin, A.V. An effect of annealing on electric properties of nanocomposites $(CoFeZr)_x(Al_2O_3)_{1-x}$ produced by magnetron sputtering in the atmosphere of argon and oxygen beyond the percolation threshold. *Prz. Elektrotech.* **2010**, *86*, 157–159.
- 26. Koltunowicz, T.N.; Zhukowski, P.; Bondariev, V.; Saad, A.; Fedotova, J.A.; Fedotov, A.K.; Milosavljević, M.; Kasiuk, J.V. Enhancement of negative capacitance effect in (CoFeZr)_x(CaF₂)_(100-x) nanocomposite films deposited by ion beam sputtering in argon and oxygen atmosphere. *J. Alloys Compd.* **2015**, *615*, S361–S365. [CrossRef]
- 27. Koltunowicz, T.N. Inductive type properties of FeCoZr–CaF₂ and FeCoZr–PZT nanocomposites. *J. Mater. Sci.-Mater. Electron.* **2015**, 26, 6450–6457. [CrossRef]
- 28. Koltunowicz, T.N.; Zukowski, P.; Boiko, O.; Saad, A.; Fedotova, J.A.; Fedotov, A.K.; Larkin, A.V.; Kasiuk, J. AC Hopping Conductance in Nanocomposite Films with Ferromagnetic Alloy Nanoparticles in a PbZrTiO₃ Matrix. *J. Electron. Mater.* **2015**, 44, 2260–2268. [CrossRef]
- 29. Koltunowicz, T.N. Dielectric Properties of (CoFeZr)_(x)(PZT)_(100-x) Nanocomposites Produced with a Beam of Argon and Oxygen Ions. *Acta Phys. Pol. A* **2014**, *125*, 1412–1414. [CrossRef]
- 30. Svito, I.; Fedotov, A.K.; Koltunowicz, T.N.; Zukowski, P.; Kalinin, Y.; Sitnikov, A.; Czarnacka, K.; Saad, A. Hopping of electron transport in granular $Cu_x(SiO_2)_{1-x}$ nanocomposite films deposited by ion-beam sputtering. *J. Alloys Compd.* **2015**, *615*, S371–S374. [CrossRef]
- 31. Mayer, M. SIMNRA User's Guide; Max-Planck-Institute fur Plasmaphysik: Garching, Germany, 1997.
- 32. Koltunowicz, T.N. Measurement Station for Frequency Dielectric Spectroscopy of Nanocomposites and Semiconductors. *J. Appl. Spectrosc.* **2015**, *82*, 653–658. [CrossRef]
- 33. Biersack, J.P.; Ziegler, J.F. The Stopping and Range of Ions in Solids; Springer: Berlin, Germany, 1982.
- 34. Zukowski, P.; Kołtunowicz, T.; Partyka, J.; Fedotova, Y.A.; Larkin, A.V. Hopping conductivity of metal-dielectric nanocomposites produced by means of magnetron sputtering with the application of oxygen and argon ions. *Vacuum* **2009**, *83*, S280–S283. [CrossRef]
- 35. Abeles, B.; Sheng, P.; Coutts, M.D.; Arie, Y. Structural and electrical properties of granular metal films. *Adv. Phys.* **1975**, 24, 407–461. [CrossRef]
- Sankar, S.; Berkowitz, A.E.; Smith, D.J. Spin-dependent transport of Co-SiO₂ granular films approaching percolation. *Phys. Rev. B-Condens. Matter Mater. Phys.* 2000, 64, 14273. [CrossRef]